



Open Archive Toulouse Archive Ouverte (OATAO)

OATAO is an open access repository that collects the work of some Toulouse researchers and makes it freely available over the web where possible.

This is an author's version published in: <https://oatao.univ-toulouse.fr/25225>

Official URL : <https://doi.org/10.1177/1475472X19890260>

To cite this version :

Serré, Ronan and Gourdain, Nicolas and Jardin, Thierry and Jacob, Marc C. and Moschetta, Jean-Marc Towards silent Micro-Air Vehicles: optimization of a low Reynolds number rotor in hover. (2019) International Journal of Aeroacoustics, 18 (8). 690-710. ISSN 1475-472X

Any correspondence concerning this service should be sent to the repository administrator:

tech-oatao@listes-diff.inp-toulouse.fr

Towards silent micro-air vehicles: optimization of a low Reynolds number rotor in hover

DOI: 10.1177/11475472X19890260

Ronan Serré , Nicolas Gourdain, Thierry Jardin, Marc C. Jacob and Jean-Marc Moschetta

Abstract

The demand in micro-air vehicles is increasing as well as their potential missions. Either for discretion in military operations or noise pollution in civilian use, noise reduction of micro-air vehicles is a goal to achieve. Aeroacoustic research has long been focusing on full scale rotorcrafts. At micro-air vehicle scales however, the hierarchization of the numerous sources of noise is not straightforward, as a consequence of the relatively low Reynolds number that ranges typically from 5000 to 100,000 and low Mach number of approximately 0.1. This knowledge, however, is crucial for aeroacoustic optimization and blade noise reduction in drones. This contribution briefly describes a low-cost, numerical methodology to achieve noise reduction by optimization of micro-air vehicle rotor blade geometry. Acoustic power measurements show a reduction of 8 dB(A). The innovative rotor blade geometry allowing this noise reduction is then analysed in detail, both experimentally and numerically with large eddy simulation using lattice Boltzmann method. Turbulence interaction noise is shown to be a major source of noise in this configuration of low Reynolds number rotor in hover, as a result of small scale turbulence and high frequency unsteady aerodynamics impinging the blades at the leading edge.

Keywords

Micro-air vehicles, blade design, noise reduction, wavy leading edge, aeroacoustic optimization

Date received: 21 July 2019; revised: 23 October 2019; accepted: 2 November 2019

Institut Supérieur de l'Aéronautique et de l'Espace (ISAE-SUPAERO), Université de Toulouse, Toulouse, France

Corresponding author:

Ronan Serré, Vestas Wind Systems, Porto Design Centre, Porto, Portugal.

Email: ronan.serre@gmail.com

Introduction

Designing a silent rotor goes through an aeroacoustic optimization, which implies understanding the aerodynamic phenomena responsible for noise generation. Predicting the noise generated aerodynamically is relatively straightforward once detailed aerodynamics involved in the propulsion system is available through the use of direct noise computation or hybrid prediction. Aeroacoustic investigations¹⁻³ or optimizations in that framework are possible^{4,5} but demanding in terms of computational cost, hence not realistic in an industrial context. To this aim, lower-fidelity tools are needed. Such models based on analytical developments seem promising⁶ although generally found in small axial fans research. A pure aerodynamic optimization of micro-air vehicle (MAV) propellers has been published by Gur and Rosen⁷ but an optimization based on both aerodynamic and acoustic characteristics has rarely been addressed although some noise reduction techniques were applied yielding promising conclusions such as an unequal blade spacing to reduce the tonal noise,⁸ boundary layer trips⁹ or trailing-edge serrations¹⁰ to remove the broadband noise. In these earlier studies, the sound was considered as mainly tonal with a broadband contribution due to the scattering of boundary layer perturbations by the blade trailing edge. The tonal part is limited to the steady loading noise as inflow distortions that are due to installation effects and inflow conditions are generally difficult to determine. The present contribution introduces an original methodology¹¹ for reducing the noise of MAV rotors while preserving or even increasing the endurance and this approach is suited for engineering purposes, from aerodynamic and acoustic prediction to shape optimization. A similar strategy has been followed by Wisniewski et al.¹² and Zawodny et al.¹³ but the models used were based on empirical data at relatively high Reynolds numbers and for symmetrical foils while analytical models are proposed and justified in the present study. From the results yielded by the optimization and comparison with measurements, backed-up with experimental and numerical further investigations, a new ranking of the noise sources in low Reynolds number rotors in hover is proposed. The paper outlines the following organization: an optimization accounting for aerodynamic power and tonal and broadband (trailing edge) acoustic components, an experimental investigation on the optimized rotor that highlighted the importance of turbulence interaction noise, investigations with numerical simulations to calibrate the modelling of the turbulence interaction noise and eventually to propose further noise reduction designs.

Numerical methodology for MAV blade noise reduction

The original methodology proposed in this study is based on simple albeit accurate analytical models for the mean radial load distribution that are coupled with an acoustic analogy and implemented into an optimization loop. The optimization algorithm can be applied at reasonable cost to two parameters among the chord, the twist and the airfoil section to the MAV blades in a multi-objective strategy.

Optimization

The optimization consists in a systematic scanning of the chosen parameter space defined by chord and twist laws as a function of the blade radius and the rotation speed with a constant thrust as objective. The blade chord and twist laws are parameterized by Bézier curves

considering control points in four sections along the blade span yielding eight variables. However, in order to ensure that lift vanishes at blade tip, which is required to minimize induced velocity, the twist at the fourth control point is set to zero thus reducing the number of variables to seven. In the combination method, each variable can take four values giving 4^7 individual evaluations. A multi-objective selection is applied to express the Pareto front that corresponds to an optimal energy consumption and an optimal overall sound pressure level. The effect of the airfoil section optimization is not addressed here but in earlier studies, it has proven to be significant.^{11,14} As a result, in the present article, an optimal blade section is chosen as basis for a chord and twist optimization according to the above mentioned objectives.

Aerodynamic modelling

For each set of parameters, the blade loading is derived from the blade element and momentum theory (BEMT) as described by Winarto.¹⁵ Distributions of lift and drag and global thrust and torque are retrieved from local lift and drag coefficients of the blade element airfoil sections. It is paramount to know the aerodynamic polar of the considered airfoil section. Three approaches may be employed to this end: experimental,¹⁶ high-fidelity simulation¹⁷ or low-fidelity modelling.¹⁸ The last one is used in the present study for its effectiveness that makes it more suitable for optimization. Lift and drag coefficients are extracted from Xfoil open-source software by Drela and Giles,¹⁸ as well as boundary layer data, using 160 panels and a low N_{crit} value typical of turbulent inflows and stored in a table look-up procedure. Xfoil is based on potential theory with viscous flow models. Xfoil results agree with experiments^{11,14} and for that reason, it is used to provide airfoil input data to the optimization tool. The aerodynamic model based on BEMT is fast and reliable but yields only steady loading on the blades. Steady loading is due to the blade acceleration and scales with the eighth power of the relative velocity: therefore it is usually outranged by unsteady loading noise in low Mach number propeller and fan applications, unless the rotor ingests steady or slowly varying flow disturbances and distortions causing the blades to feel unsteady loading as they cross these disturbances. Both steady and low frequency unsteady loading radiate at multiples of the blade passing frequency, that is the shaft speed frequency multiplied by the number of blades. Unsteady disturbances might produce additional broadband noise if they are shortly correlated in space. Unsteady loading is a much more efficient noise source than steady loading noise at moderate Mach numbers, since it varies with the sixth power of the flow velocity. Unsteady loading sources can be due either to upstream disturbances that produce interaction noise near the leading edge or to disturbances shed by the blades that cause trailing edge noise, which is generated by a trailing edge scattering mechanism: this mechanism is less efficient than turbulence/leading edge interaction noise. Trailing edge noise is either fed by boundary layer turbulence in which case it is of broadband nature or to trailing edge vortex shedding that is mainly tonal. Additional tonal sources might occur if the blades cross the potential field of a downstream located obstacle or if the boundary layer is transitional and undergoes a Tollmien–Schlichting feed-back mechanism. If the blades are not unsteadily loaded, except maybe for broadband trailing edge noise, the steady loading becomes of primary importance even at low speeds. Another type of source might then also play a role, the sound power of which scales with the eighth power of the velocity: thickness noise. Unsteady tonal loading noise might be relatively easily predicted if the associated flow perturbations are known, which is unfortunately

not always the case, especially for open rotors, which are very sensitive to ingested vortical disturbances. These are very difficult to predict as their presence is bound to the environment.¹⁹ However, in some particular situations, such as in confined environments, these perturbations might be due to the rotor wakes recirculating in the domain and are within reach of modern unsteady flow simulations.²⁰ These unsteady sources are not modelled in the optimization process as their prediction requires significant computational resources. Thus, only trailing edge noise, which can be estimated with statistical models given a few flow assumptions, is added to the steady loading noise prediction.

Acoustic modelling

The acoustic modelling is performed in two steps: (i) an integral method based on the Ffowcs Williams and Hawkins²¹ (FWH) equation gives the tonal noise radiated by the rotor from the steady loading yielded by the BEMT and (ii) analytical models estimate the broadband part of the acoustic spectrum based on the work of Roger and Moreau.²² The FWH equation is implemented in the time domain in the form known as Formulation 1A²³ and applied on the blade surface.²⁴ The quadrupole term is removed from the FWH equation and since the integration surfaces correspond to the blades, no quadrupole source is taken into account. This is physically consistent with the low Mach number range of the MAV rotors.²⁵ As a consequence, the FWH integral reduces to thickness and loading noise computation obtained from the two surface integrals, the unsteady part of which being restricted to the blade boundary layer fluctuations. The main input parameters are the incoming flow velocity at the blade element influencing the thickness noise and the force distributions acting on the loading noise. In that steady loading framework, the latter is found to be relatively small without significantly contributing to the overall noise while the former is found to be dominant independently of the observer's location. In addition, one source of broadband noise is considered, as being initially thought as predominant¹⁰: the noise due to the scattering of the boundary layer disturbances at the trailing edge. This noise component has been modelled by Roger and Moreau.²² Furthermore, the Doppler effect due to the relative motion between the source and the observer is also accounted for.²⁶ The main inputs for this model are the wall pressure spectrum and the spanwise coherent length and both can be modelled from boundary layer data. The convection velocity, which is the third significant parameter, is set to 60% of the inflow velocity. Boundary layer information is obtained from the Xfoil software as discussed in Serré et al.¹¹ The spanwise correlation length is approximated using Corcos model²² with high-pass filtering. The wall pressure spectrum is modelled from Kim and George²⁷ based on a review by Blandeau.²⁸ Moreover, this model, which is commonly used for rotor blades, accounts for the airfoil geometry.

Optimized rotor

The optimization tool is used to determine a low noise blade geometry for an actual, albeit experimental, tilt-body MAV developed at ISAE-SUPAERO named 'MAVion' with two rotors in tandem.²⁹ The original rotors are two-bladed with APC7 × 5 commercial blades. In the optimization process, chord and twist distribution laws are derived from a range of possibilities in the spanwise chord–twist space for several numbers of blades per rotor at a given thrust of 2.85 N required for hovering flight, allowing for the rotational speed to

adjust. The rotor tip radius is however imposed to match the case of the APC7 × 5 blades, that is $R = 0.0875$ m. The airfoil section is a thin, cambered Goettingen 265, suitable for low Reynolds number flow. Since the airfoil section of APC7 × 5 blades was unknown to the authors, the conventional and the optimized rotors are compared experimentally. The optimized rotors are manufactured using SLA technology on a 3D printer with a $50\ \mu\text{m}$ vertical resolution such as depicted in Figure 1. The printed rotors are manually grinded to smooth out any remaining surface roughness and are balanced on a static equilibrium axis. The maximum noise reduction measured for the optimized geometries is achieved by the three-bladed configuration. Its chord and twist distribution laws are plotted in Figure 2 along with those of the conventional rotor. The radial position is normalized by the tip radius $R = 0.0875$ m. The twist angle β is defined with respect to the plane of rotation (without pitch angle). The optimized chord is larger than that of the conventional rotor whereas the twist laws are approximately the same, except at 75% of blade span where the optimized twist increases again before vanishing at the tip. The optimized geometry is proposed for free download^a in the form of an STL file to serve as a benchmark case.



Figure 1. Optimized rotor, 3D printed with SLA technology. Sources: Usine Nouvelle [copyright].

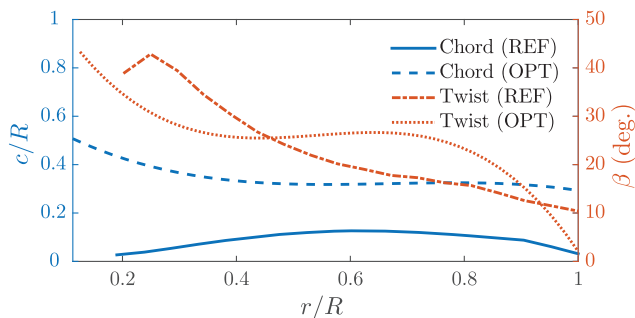


Figure 2. Chord and twist distribution laws for the conventional rotor ('REF') and the optimized rotor ('OPT'). Normalized by tip radius $R = 0.0875$ m.

Experiments

Aerodynamic measurements

The aerodynamic forces were retrieved from a five-component balance. Comparisons between the aerodynamic performance of the conventional and the optimized rotor are shown in Figure 3: the thrust coefficient and the figure of merit are plotted in Figure 3(a) and (b), respectively. The thrust coefficient C_t and the figure of merit FM are defined according to Leishman³⁰ as

$$C_t = \frac{T}{\frac{1}{2}\rho(\omega R)^2\pi R^2} ; \quad FM = \frac{T^{3/2}}{\omega Q\sqrt{2\rho\pi R^2}} \quad (1)$$

where T is the thrust, ρ is the ambient density, ω is the rotational frequency and R is the rotor tip radius. The thrust objective is reached at approximately 5400 r/min versus 8500 r/min for the conventional rotor (Figure 3(a)). The figure of merit is higher for the optimized rotor than for the conventional one (Figure 3(b)) although it is decreasing with the rotational speed for the optimized rotor while increasing for the conventional rotor. When the thrust objective is reached the optimized rotor has a figure of merit 1.3 times higher than the conventional rotor whereas the thrust coefficient is 3 times higher (Figure 3(a)). This indicates that the optimized rotor is aerodynamically more efficient.

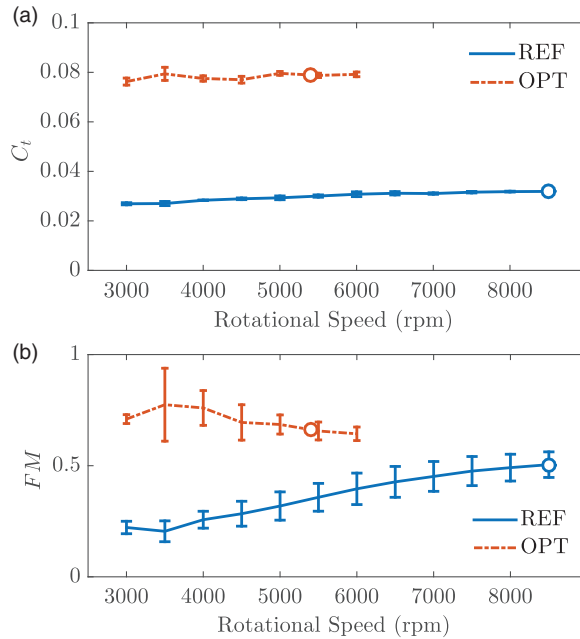


Figure 3. Aerodynamic performance. Conventional rotor ('REF') and optimized rotor ('OPT'). Blank symbols indicate value at thrust objective. Measurements with standard deviation. (a) Thrust coefficient and (b) figure of merit.

Acoustic measurements

The measurements took place in a rectangular room of dimensions $(l_1 \times l_2 \times l_3) = (14.9 \times 4.5 \times 1.8) \text{ m}^3$. Because the room is not acoustically treated, the sound power level is computed according to ISO 3746:1995 standard with five measurement points 1 m around the rotor, on a Brüel & Kjær 1/2 in. free-field microphone and a Nexus frequency analyser with a frequency resolution of 3.125 Hz. The distance between the source and the microphones approximately represents 5 rotor diameters. Four of the microphones are positioned in the form of a circle parallel to the ground, the centre of which is aligned with the rotor centre of rotation. The fifth microphone is located in the plane of rotation, that is vertical. A reduction of 8 dB(A) in the acoustic power is observed between the conventional rotor and the optimized one at the thrust objective (Figure 4). At same rotational speed however, the optimized rotor radiates more acoustic energy.

At 4500 r/min, the standard deviation is particularly high for the optimized rotor. This is probably due to flow separation or installation effects: Figure 5 shows a close-up view of the experimental set-up. The rotor is close to the ground which might trigger the ingestion of vorticity filaments by the rotor causing distortion effects. From typical narrow band measurements of both rotors (Figure 6), sound power reduction is achieved through reduction in both tonal and broadband parts of the acoustic spectrum. The mid frequency harmonics (between 2000 and 6000 Hz) have been significantly reduced and even removed in some cases (Figure 6). It is difficult to identify a specific noise source mechanism in the measured acoustic spectrum for several reasons: (i) the inflow has not been characterized and distortion effects might be expected and (ii) the ISO 3746:1995 standard estimates acoustic power for non-anechoic environments but a single acoustic pressure spectrum still includes reflections and external noise. Moreover, the experimental test bench holds the rotor in such a way that its axis of rotation is parallel to the ground (Figure 5). As a consequence, a stand that includes the aerodynamic balance is mounted vertically, behind the rotor, eventually yielding unsteady loading on the blades creating more additional noise radiation at the blade passing frequencies, or even between the blade passing frequencies as observed for the baseline rotor. These particular peaks might be due to asymmetry in the geometry or in the balance of the baseline, commercial rotor. In addition, the motor radiates its own noise. A sharp tonal peak can be identified on narrow band measurements at a passing frequency based on the number of magnetic poles in the motor but broadband noise possibly yielded by the motor has not been identified so far. The methodology described aims at identifying a

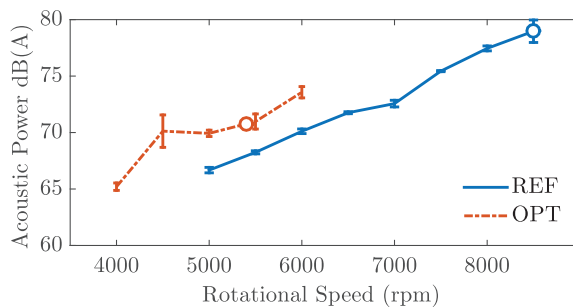


Figure 4. Acoustic power. Conventional rotor ('REF') and optimized rotor ('OPT'). Blank symbols indicate value at thrust objective. Measurements with standard deviation.

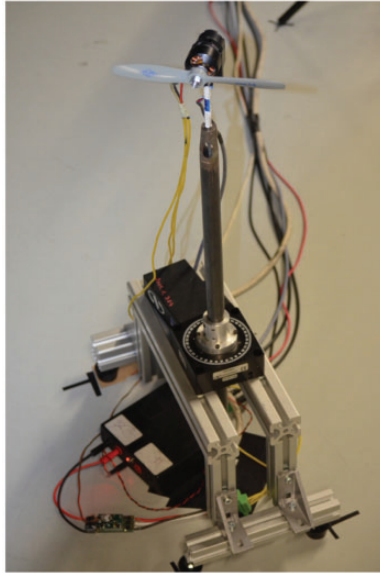


Figure 5. Close-up view of the experimental set-up.

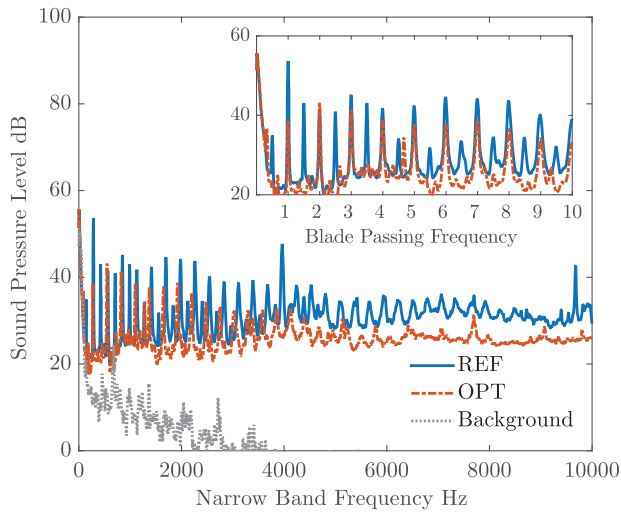


Figure 6. Acoustic spectra for the conventional rotor ('REF') and the optimized rotor ('OPT') at the rotational speed of the thrust objective. The spectra are averaged over microphone positions and measurement sessions. Close-up view with frequencies normalized by the blade passing frequency.

relative noise reduction by evaluating every rotor in the same conditions. The optimization tool has proven its effectiveness to propose an innovative geometry achieving noise reduction while increasing endurance. However, as previously mentioned, at this early stage of development the optimized rotor was obtained under the assumption that trailing edge noise

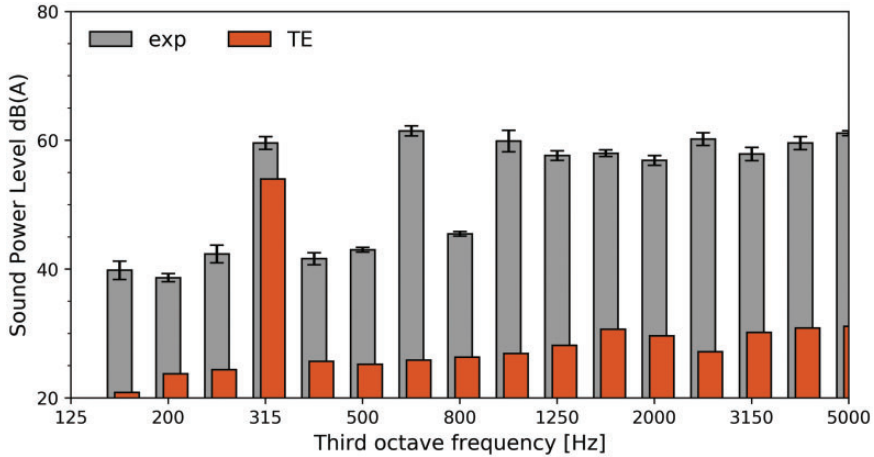


Figure 7. Comparison in sound power level (ISO 3746:1995 standard) between measurement ('exp') and numerical prediction from the optimization tool with trailing edge noise modelling ('TE'). Rotational speed of the thrust objective.

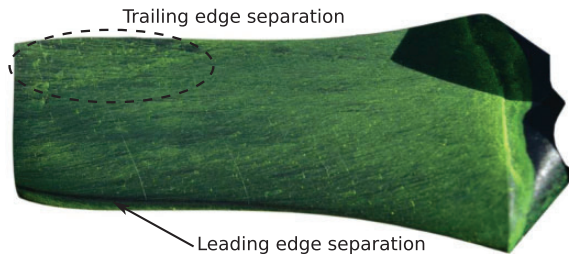


Figure 8. Oil flow visualization (viscous coating) on a blade of the optimized rotor at 5000 r/min. The blade is seen from the suction side with the leading edge underneath the trailing edge.

was the unique source of broadband noise. The prediction from the optimization tool is compared in Figure 7 with noise measurements at the rotational speed of the thrust objective. The tonal component is relatively well captured (in the 315 Hz frequency band which contains the blade passing frequency), a few decibels notwithstanding that can be accounted for by installation effects, as previously discussed. A significant part of the broadband spectrum in the high frequency region is missing from the prediction. Experimental evidence of the aerodynamic behaviour that could indicate the nature of that missing high frequency, broadband source of noise is discussed hereafter.

Oil flow visualization

To identify the occurrence of specific patterns in the flow structures, a viscous coating has been applied on a blade's suction side of the optimized rotor and tested at 5000 r/min. The result presented in Figure 8 shows mainly the entrainment of oil particles by centrifugal force. However, two observations are worth noting. First, a leading edge separation clearly

occurs very early. It is made visible by the absence of oil particles due to the low pressure induced by the separation. Immediately after that leading edge separation, the transition of the boundary layer from laminar to turbulent occurs and is probably triggered by the impingement of wake turbulence. Second, a separation occurs at the trailing edge. It takes its energy from the merging of the leading edge separation and the tip vortex and is shed in the wake to constitute most of the turbulence that in turn impinges on the following blade's leading edge. As discussed in the next section, this visualization is consistent with the wake–blade interaction evidenced by a high-fidelity numerical simulation. Such an interaction also provides a good candidate source mechanism to explain the discrepancy between the trailing edge noise prediction and the measured broadband noise spectrum shown in Figure 7. Roger and Moreau²² proposed a generalized semi-analytical interaction noise model based on a linearized theory following the work of Amiet.³¹ Among other inputs, this model requires an estimate of the incoming turbulence length scales and characteristics. They can either be obtained experimentally or via an unsteady flow simulation as shown in the next section.

Characterization of turbulence ingestion with higher fidelity numerical method

Numerical set-up

In order to estimate the incoming turbulence, a large eddy simulation based on the lattice Boltzmann method, hereafter referred to as LES–LBM, is carried out. Additionally to its computational performance, the main advantage of LES–LBM is that the method is stable without artificial dissipation, which makes it equivalent to solve the Navier–Stokes equations with a high-order numerical scheme.³² In a recent study,³³ such a strategy has been identified as a good candidate to estimate turbulence length scales and is used now for the same reason. The present discretization of the equations ensures that the method is second-order accurate both in time and space. The main equations are solved using the open source software Palabos (www.Palabos.org) on a cubic domain with an edge of about $45R$. The mesh of the rotor is composed of 249 million Cartesian cells with decreasing size when approaching the rotor. Boundary conditions are coupled with a buffer layer of 1 m to minimize spurious reflections. The dimension of the first cell layer at the rotor wall is $350\ \mu\text{m}$ to obtain a y^+ of 50 in the tip region. Hence, y^+ values along the span are always below 50. One rotor revolution is achieved in 250 and 16,000 time steps in regions with coarse and fine grids, respectively, and data are extracted after eight revolutions. In addition, it was verified that the results are converged with respect to the typical cell size.³³ Analysing the characteristics of the optimized geometry with such a numerical method is justified by its capacity to accurately estimate correlation lengths³³ and by the possibility to investigate unsteady aerodynamic behaviour, calibrate the broadband noise models in the optimization tool and eventually give insight for low noise design solutions (such as vortex generators or edge treatments). An unsteady behaviour occurs around 75% of the blade radius, where the twist angle increases again (Figure 2) suggesting that having an inflection point on the twist distribution law should probably be avoided. The resulting flow then merges with the tip vortex and impinges the following blade. In addition to the previous evidences experimentally obtained, this also contributes to suggest the presence of interaction noise and its importance in the hierarchy of sources of noise in this configuration.

Correlation lengths and turbulence length scales

Several length scales can be used to quantify turbulence: the integral scale L , the Taylor microscale λ_g and the Kolmogorov scale η . These length scales are illustrated in Figure 9 on a turbulent boundary layer. The Taylor microscale appears relevant to describe turbulence impinging a leading edge with a wake characterized by a sub-critical Rossby number,³³ identifying a region where vortex breakdown is likely to occur and inducing strong rotational effects. The Taylor microscale is representative of the actual length the leading edge will see when hit by turbulent structures^{34,35} (Figure 9). The Taylor microscale is deduced from the two-point correlations defined as³⁷

$$B_{ij} = \frac{\overline{V_i(r_1, t) \cdot V_j(r_2, t)}}{\sqrt{\overline{V_i^2(r_1, t)}} \cdot \sqrt{\overline{V_j^2(r_2, t)}}}$$

with r_1 and r_2 being two positions along the rotor span. The overline stands for temporal averaging. Here, the correlation is considered in the spanwise direction (from the tip to the root of the rotor) using the azimuthal component of the velocity V_θ according to referential frame shown in Figure 10. The two-point correlation functions can be estimated for the different components of the velocity in the rotor frame (B_{zz} , $B_{\theta\theta}$, B_{rr}) and the static pressure (B_{pp}). The results are presented in Figure 11, upstream the rotor leading edge at $r/R = 0.75$. The correlation function shows the same behaviour for the three velocity components but the correlation length increases by a factor 2 when considering the static pressure p . This is consistent with the fact that pressure signals are correlated over a longer distance than velocity signals. In the reference frame of the rotor, the main component of the velocity is the azimuthal component, so the spanwise correlation function is defined as $g(r) = B_{\theta\theta}$. From such information it is possible to deduce the Taylor microscale λ_g , knowing the second

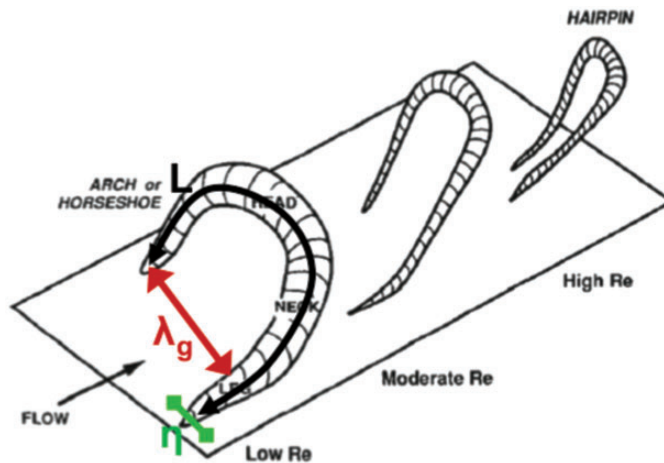


Figure 9. Illustration of turbulence length scales in a turbulent boundary layer from Robinson³⁴ after Head and Bandyopadhyay.³⁵ Source: Reproduced from Gourdain et al.³⁶

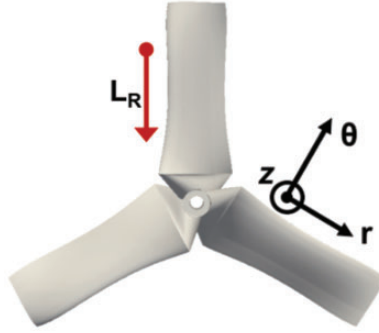


Figure 10. Coordinates system used for computation of the correlation lengths.

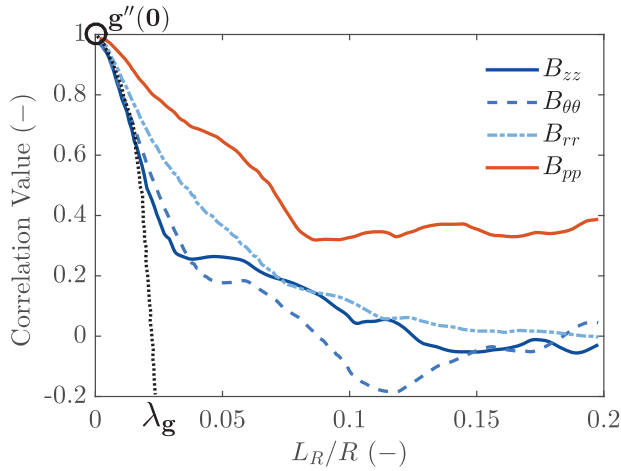


Figure 11. Normalized correlation length L_R/R upstream the rotor leading edge at $r/R=0.75$.

derivative of the correlation function at $L_R/R=0$

$$\lambda_g^2 = -\frac{2}{g''(0)} \quad (2)$$

Close to the origin, it is possible to express the correlation function in terms of a McLaurin series. By retaining only the first-order term, the correlation function writes at the origin

$$g(L_R) = 1 - \frac{L_R^2}{\lambda_g^2} \quad (3)$$

From equation (3), it is easy to estimate the Taylor microscale λ_g as depicted in Figure 12 in a plane located at 0.3 chord upstream of the rotor leading edge. The typical value of λ_g evolves from $0.02R$ (internal part of the shear layer) to $0.03R$ (external part of the shear

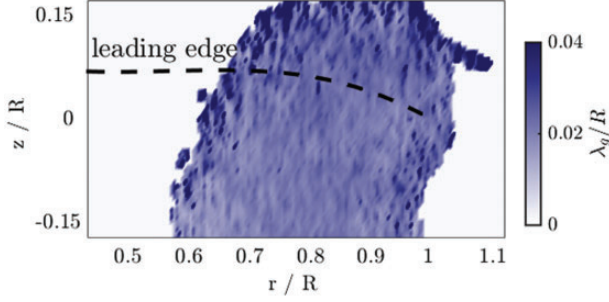


Figure 12. Taylor microscale λ_g upstream of the leading edge of the optimized rotor normalized by maximum radius. LES–LBM simulation.

layer, close to the tip). Two comments can be done regarding this value: (i) a very fine grid is required to properly estimate the Taylor microscale, the typical grid dimension should be one order of magnitude lower than this length scale, so the present grid is at the limit of this requirement with $\Delta = 0.002R$ and (ii) the value of λ_g is roughly constant all over the rotor span, which is an interesting point since it means that a control solution or an optimized design will have to deal with only one typical length scale which led the authors to seriously consider wavy leading edges as a passive noise reduction device. The turbulence appears to be relatively homogeneous both in the vertical direction (z/R) and in the radial direction (r/R) between 60 and 90% of the blade radius.

Extension of the broadband noise modelling in the optimization tool

The discussion about the numerical and experimental results in the previous section strongly suggests that interaction noise plays a major role in the present low Reynolds number hovering rotor. Therefore, an interaction noise model is included in the optimization tool using a similar formalism as for the trailing edge noise.²² The interaction noise is seen to be proportional to the two-dimensional wavenumber cross-spectrum of the upwash velocity fluctuations ϕ_{ww} integrated over all spanwise hydrodynamic wavenumbers. In the optimization tool used in the present study, such detailed information is not accessible. It is however possible to model this quantity based upon the turbulence length scale and turbulence intensity of the chordwise velocity fluctuation. The model proposed by von Kármán as cited in Amiet³¹ is used. As already discussed, in the present study the Taylor microscale λ_g is chosen instead of the integral length scale.²² λ_g is derived from the LES–LBM simulation. In order to apply the optimization tool, the length scale needs to be estimated differently as LES–LBM simulations are too expensive to be included in an optimization loop. For this purpose, further assumptions and approximations are required. Assuming a clean rotor inflow, the turbulence impinging the leading edge is subsequently generated by the wake of the trailing edge of the previous blade, as it is believed to be separated according to the simulation results. A similitude is thus expected between leading edge turbulence and trailing edge wake. The boundary layer information from Xfoil is used to estimate the width of the wake near 90% of the chord according to the definition proposed in Fukano et al.³⁸

$$D_w^* = d_{AS} + \delta_p^* + \delta_s^* \quad (4)$$

where d_{AS} is the airfoil section thickness near the trailing edge and δ_p^* and δ_s^* are the boundary layer displacement thicknesses on pressure side and suction side, respectively. A comparison between the turbulence length scale measured from the LES–LBM simulation upstream of the leading edge and an estimate of the wake width from the numerical tool is plotted in Figure 13. It is unknown whether that scaling is relevant in every situation before further investigations are carried out but a helpful agreement is observed. For the following optimizations, the turbulence length scale is estimated from the Xfoil software based on boundary layer data and equation (4) to feed the ϕ_{ww} models. For the following computations, a value of 4 m/s for the intensity of the chordwise velocity fluctuation is found in the LES–LBM simulation, representing 10% of the tip speed. The same comparison as previously shown in Figure 7 is now reproduced in Figure 14 with the addition of the turbulence interaction noise prediction. The modelling of the turbulence interaction noise

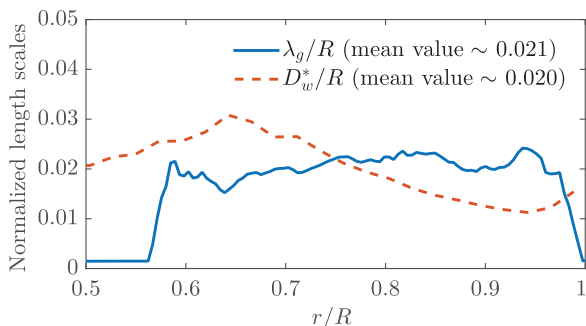


Figure 13. Comparison of length scales representative of turbulence and wake. λ_g predicted from LES–LBM simulation and D_w^* predicted from the optimization tool. Normalized by tip radius.

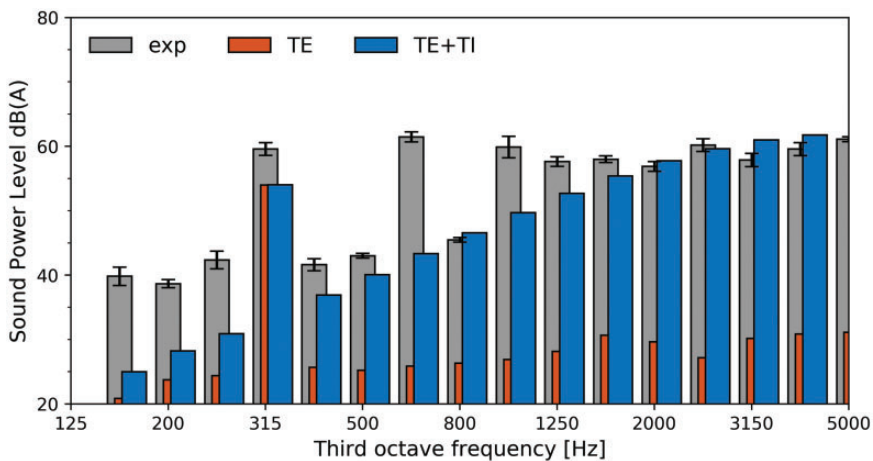


Figure 14. Comparison in sound power level (ISO 3746:1995 standard) between measurement ('exp') and numerical prediction from the optimization tool with trailing edge noise modelling ('TE') and with the addition of the turbulence interaction noise modelling ('TE+TI'). Rotational speed of the thrust objective.

allows the optimization tool prediction to reach the levels measured. This is the final evidence suggesting that interaction noise is a dominant source of noise in the hovering flight of MAV, as a result of rapid lift variations induced by the ingestion of small scales of turbulence.

Interacting on the leading edge

After observing that interaction noise is the dominant source of noise for a MAV rotor in hover and that it is produced by wake turbulence impinging the leading edge, it can be expected that a suitable leading edge treatment is likely to reduce the noise radiation. For instance, wavy leading edges which have been investigated in the early 1970s³⁹ have recently received a regain of interest.⁴⁰⁻⁴⁵ However, none of these recent studies were applied to rotating blades. A parametric study has been carried out yielding three specific designs hereby considered, among which two were investigated in LES-LBM simulations. These designs have a chord distribution law that is modulated by a sine function characterized by a wavelength λ and an amplitude A . The phase of the sine function has not been considered. The first design is labelled ‘LWL’ that stands for *Large WaveLength* and was inspired by Favier et al.⁴⁰ The second design is labelled ‘TWLM’ that stands for *Taylor Wavelength Maximum* while the third design is labelled ‘TWLm’ for *Taylor Wavelength minimum*. These two last designs were inspired by Chaitanya et al.⁴³ that suggest the wavelength of the chord modulation should scale with the turbulence length scale without referring to a specific length scale. As discussed earlier in this contribution, the Taylor microscale is considered as the length scale driving the acoustic response to turbulence ingestion noise and is then used to scale the leading edge designs. The wavelength and amplitude for each of those three designs are summarized in Table 1 and the corresponding chord distribution laws are plotted in Figure 15. The wavy leading edges are applied to the optimized rotor previously described that is now referred to as the baseline.

The thrust coefficient C_T , the figure of merit from equation (1) and the sound power according to ISO 3746:1995 standard were measured for the three wavy leading edge designs and compared with the baseline at two rotational speeds. Note that 5000 r/min is the closest value to the thrust objective of the optimized rotor while 3000 r/min is an additional arbitrary value. Results are summarized in Table 2. From Table 2 it can be observed that the thrust coefficient is almost constant although slightly higher for the ‘TWLM’ design but in that particular case, the figure of merit is seen to dramatically decrease indicating an increase in torque. The ‘LWL’ design has a higher figure of merit and a lower acoustic power. This is more pronounced with the ‘TWLm’ design. Lower amplitudes seem to provide satisfactory results. When associated with the lower wavelength, the best results are achieved. However,

Table 1. Wavelengths and amplitudes for the wavy leading edges applied on the optimized rotor.

	LWL	TWLM	TWLm
λ	$\sim C$	$\sim 4\lambda_g$	$\sim 4\lambda_g$
A	$\sim 0.07C$	$\sim 0.14C$	$\sim 0.04C$
Source	Favier et al. ⁴⁰	Chaitanya et al. ⁴³	Chaitanya et al. ⁴³

LWL: Large WaveLength; TWLm: Taylor Wavelength minimum; TWLM: Taylor Wavelength Maximum.

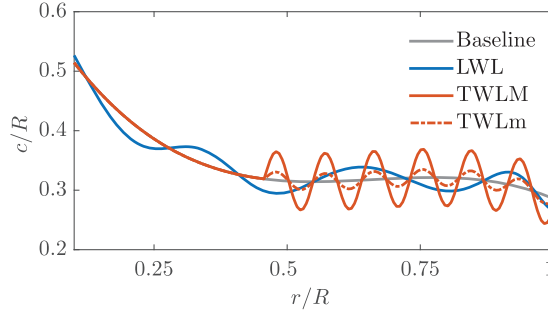


Figure 15. Chord distribution laws for wavy leading edges of different wavelengths and amplitudes. LWL: Large WaveLength; TWLm: Taylor Wavelength minimum; TWLM: Taylor Wavelength Maximum.

Table 2. Aerodynamic performance and acoustic power of the wavy leading edge designs and the baseline optimized rotor.

		Baseline	LWL	TWLM	TWLm
3000 r/min	C_t	0.08	0.08	0.09	0.08
	FM	0.71	0.65	0.50	0.73
	L_{wA}	–	–	–	–
5000 r/min	C_t	0.08	0.08	0.10	0.08
	FM	0.69	0.76	0.57	0.82
	L_{wA}	69.9	69.3	72.2	68.8

LWL: Large WaveLength; TWLm: Taylor Wavelength minimum; TWLM: Taylor Wavelength Maximum.

The numbers in TWLM highlights the design with lower efficiency and higher noise.

The numbers in TWLm highlights the design with higher efficiency and lower noise.

results from numerical simulation may mitigate these preliminary conclusions. The Q-criterion coloured by the axial velocity is plotted in Figure 16 for the baseline optimized rotor (Figure 16(a)) and the ‘LWL’ design (Figure 16(b)). As previously discussed and as was observed on the oil flow visualization shown in Figure 8, a leading edge separation also occurs in the numerical simulation near 70% of the tip radius which the wavy leading edge seems to reduce. Figure 17 also suggests that wavy leading edges can yield improvements on another sound mechanism by reducing the pressure fluctuations at the trailing edge. It seems from Figure 17 that the ‘TWLM’ design is not as interesting as what can be expected from the experimental results (Table 2). The area of high pressure fluctuations is stronger in this case than for the ‘LWL’ design but contained in a narrower region. However, it is reminded that the trailing edge noise is not believed to be of significant contribution to the acoustic power. A specific design of wavy leading edge might strengthen the pressure fluctuations at the trailing edge but still be able to radiate less total acoustic energy unless if pressure fluctuations at the trailing edge drive the turbulence intensity and turbulence length scales impinging on the following leading edge. In Figure 18 is plotted Q-criterion coloured by the normalized turbulent kinetic energy on the suction side of the three designs applied on the optimized rotor. The wavy leading edges have clearly reduced the activity of the turbulent eddies that separate near the leading edge and that is more effective with the ‘TWLm’ design. That is consistent with the experimental observation summarized

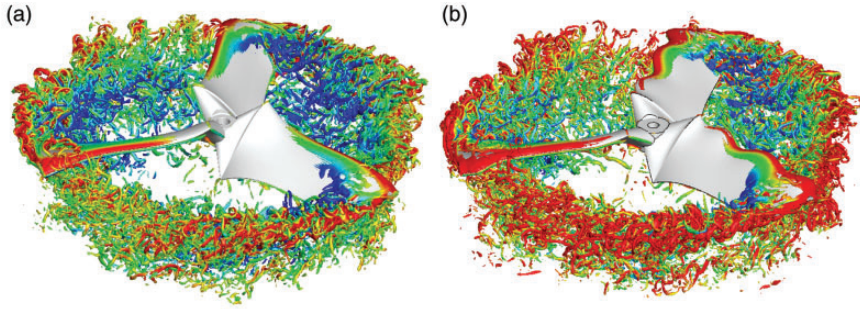


Figure 16. Iso-surface of Q-criterion coloured by axial velocity for the optimized rotor at 5000 r/min. LES–LBM simulation. (a) Baseline and (b) 'LWL' design.

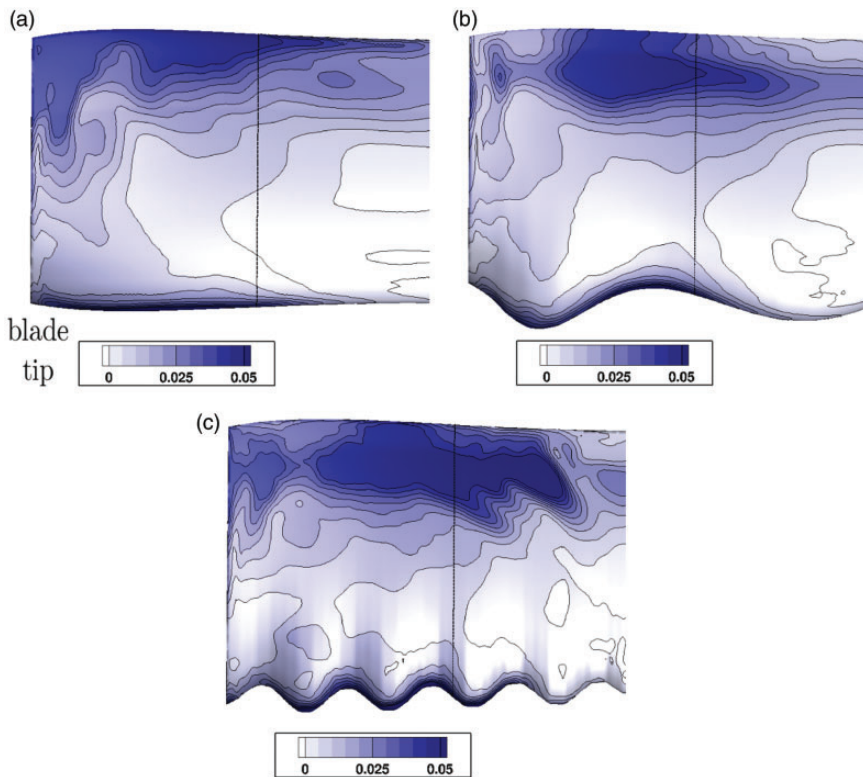


Figure 17. Static pressure normalized by $1/2 \times (\omega R)^2$ on the suction side of the optimized rotor at 5000 r/min. LES–LBM simulation. The blade tip is on the left side of the figures. (a) Baseline, (b) 'LWL' design and (c) 'TWLm' design.

in Table 2. In that case, the kinetic turbulent energy seems to spread on a wider range along the rotor radius eventually creating additional turbulent activity near the mid-span region. The wavy leading edge designs investigated in the present study are found to be more effective for large wavelength and low amplitudes: they do not act directly on the turbulence

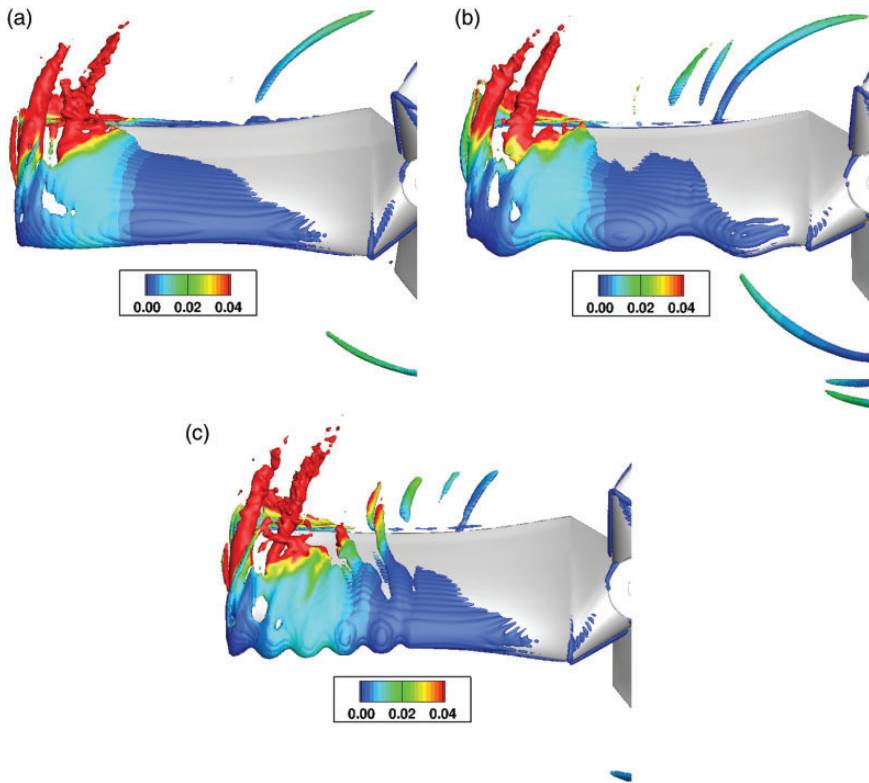


Figure 18. Iso-surface of Q-criterion coloured by turbulent kinetic energy normalized by $1/2 \times (\omega R)^2$ for the optimized rotor at 5000 r/min. LES-LBM simulation. (a) Baseline, (b) 'LWL' design and (c) 'TWLm' design.

interaction noise as an acoustic filter but indirectly by delaying separation, affecting the wake then subsequently mitigating the interaction noise as a consequence.

Conclusion

An optimization tool has been applied to reduce the noise and increase the endurance of a hovering MAV. The methodology is mainly based on low-order computational tools for the estimation of aerodynamic steady loading, tonal and broadband noise and is coupled with optimization algorithms for modifications of chord and twist radial distribution laws. This approach is suitable for engineering purposes and makes rotor optimization for quiet and enduring MAVs realistic in an industrial context. Reducing the noise from MAVs in hover can be achieved without expensive means. High-order computational tools could then be applied to study further reduction of noise levels. An 8 dB(A) reduction of the sound power was measured with an experimental protocol suitable for non-anechoic environments. It was obtained by increasing the number of blades and optimizing the chord and twist distributions for a given thrust and a given rotor radius. The noise reduction is mainly due to the resulting shaft speed reduction at iso-thrust. The optimized geometry

is open for free download to serve as a benchmark case. Further reduction of noise levels is expected in the future using the tools presented in this paper. Results analysed and discussed in the present article bring new insights in the noise source ranking of low Reynolds number rotor in hover. Tonal noise at the blade passing frequency is an important source of noise and is then driven by the rotational speed. The optimization tool allows tonal noise reduction by shape optimization to increase the aerodynamic efficiency that reduces the rotational speed. However, a major result which was confirmed by LES–LBM simulation is that the dominant source of noise is due to the wake-leading edge interaction of neighbouring blades. On the other hand, trailing edge noise is found to be of secondary importance. Turbulence interaction emerges from lift variations caused by the impingement of turbulent eddies at the blade's leading edge. It has been emphasized the importance of the careful selection of the representative length scale of the inflow turbulence. In the context of a low Reynolds number rotor in hover, the use of Taylor microscale is suggested. The turbulence impinging the leading edge is found to be relatively homogeneous in the numerical simulations and since most of the noise is produced in the leading edge region, a specific design was expected to significantly reduce acoustic radiation by destroying homogeneous turbulence or by allowing phase cancellation of the acoustic waves resulting from the scattering of turbulence wavelength by the leading edge. For that purpose, several wavy leading edges were tested both experimentally and numerically. However, there is still no clear consensus on the optimum chord modulation in terms of wavelength and amplitude and the present study did not cover a large enough range of parameter values to conclude on this point. In the context of steady loading, turbulence interaction noise occurring with straight leading edges can be estimated by broadband noise models but an accurate modelling of aerodynamic unsteadiness that could improve prediction is discarded for rotor optimization by the resulting computational costs. The methodology proposed in this contribution is then a reasonable strategy. The modelling of another source of broadband noise produced by vortex shedding on the blade's suction side has been left for future work but could be investigated following the procedure described in the present paper.

Acknowledgements

The authors thank the technical team for the experimental support and specially Rémy Chanton from for the set-up of the aerodynamic balance, Sylvain Belliot for the rapid prototyping and Henri Dedieu for the oil flow visualization.

Declaration of conflicting interests

The author(s) declared no potential conflicts of interest with respect to the research, authorship, and/or publication of this article.

Funding

The author(s) disclosed receipt of the following financial support for the research, authorship, and/or publication of this article: This work has been partly supported by the French Procurement Defense Agency under grant DGA/MRIS no. 2012.60.0012.

ORCID iD

Ronan Serré  <https://orcid.org/0000-0003-4970-0780>

Note

a. ftp://depozit.isae.fr/ISAE_MAVion_NB3.stl.

References

1. Rama Krishna S, Rama Krishna A and Ramji K. Reduction of motor fan noise using CFD and CAA simulations. *Appl Acoust* 2011; 72: 982–992.
2. Park M and Lee D. Sources of broadband noise of an automotive cooling fan. *Appl Acoust* 2017; 118: 66–75.
3. Wang C. Noise source analysis for two identical small axial-flow fans in series under operating condition. *Appl Acoust* 2018; 129: 13–26.
4. Pagano A, Barbarino M, Casalino D, et al. Tonal and broadband noise calculations for aeroacoustic optimization of propeller blades in a pusher configuration. *J Aircraft* 2010; 47: 835–848.
5. Pednekar S, Ramaswamy D and Mohan R. Helicopter rotor noise optimization. In: *The 5th Asian-Australian Rotorcraft Forum*.
6. Santos Borges S, Zdansky PSB and Barbieri R. A hybrid analytical/experimental model for evaluation of the aerodynamic noise in fans. *Appl Acoust* 2015; 90: 81–87.
7. Gur O and Rosen A. Optimization of propeller based propulsion system. *J Aircraft* 2009; 46: 95–106.
8. Cattanei A, Ghio R and Bongiovi A. Reduction of the tonal noise annoyance of axial flow fans by means of optimal blade spacing. *Appl Acoust* 2007; 68: 1323–1345.
9. Leslie A, Wong KC and Auld D. Broadband noise reduction on a mini-UAV propeller. In: *The 14th AIAA/CEAS aeroacoustics conference*.
10. Pagliaroli T, Camussi R, Candeloro P, et al. Aeroacoustic study of small scale rotors for mini drone propulsion: serrated trailing edge effect. In: *AIAA/CEAS aeroacoustics conference*.
11. Serré R, Pichon N, Fournier H, et al. A design methodology for quiet and long endurance MAV rotors, international journal of micro air vehicles. *Int J Micro Air Veh* 2019; 11: 1–14.
12. Wisniewski CF, Byerley AR, Heiser WH, et al. Designing small propellers for optimum efficiency and low noise footprint. In: *The 33rd AIAA applied aerodynamics conference*, paper no. AIAA-2015-2267.
13. Zawodny NS, Douglas Boyd JD and Burley CL. Acoustic characterization and prediction of representative, small-scale rotary-wing unmanned aircraft system components. In: *The 72nd AHS Annual Forum*.
14. Serré R, Chapin V, Moschetta JM, et al. Reducing the noise of micro-air vehicles in hover. In: *International micro aerial vehicle conference*.
15. Winarto H. *BEMT algorithm for the prediction of the performance of arbitrary propellers*. Melbourne: The Sir Lawrence Wackett Centre for Aerospace Design Technology, Royal Melbourne Institute of Technology, 2004.
16. Lyon CA, Broeren AP, Giguère P, et al. *Summary of low-speed airfoil data volume 3*. Virginia Beach, VA: SoarTech Publications, 1998.
17. Morgado J, Vizinho R, Silvestre MAR, et al. XFOIL vs CFD performance predictions for high light low Reynolds number airfoils. *Aerosp Sci Technol* 2016; 52: 207–214.
18. Drela M and Giles MB. Viscous-inviscid analysis of transonic and low Reynolds number airfoils. *AIAA J* 1987; 25: 1347–1355.
19. Sturm M and Carolus T. Impact of the large-scale environment on the tonal noise of axial fans. *Proc IMechE, Part A: J Power and Energy* 2013; 227: 703–710.
20. Casalino D, van der Velden W, Romani G, et al. Aeroacoustic analysis of urban air operations using the LB/VLES method. In: *AIAA/CEAS aeroacoustics conference*.
21. Ffowes Williams JE and Hawkings DL. Sound generation by turbulence and surfaces in arbitrary motion. *Philos Trans R Soc Lond* 1969; 264: 321–342.

22. Roger M and Moreau S. Extensions and limitations of analytical airfoil broadband noise models. *Int J Aeroacoust* 2010; 9: 273–305.
23. Farassat F and Succi GP. A review of propeller discrete frequency noise prediction technology with emphasis on two current methods for time domain calculations. *J Sound Vib* 1980; 71: 399–419.
24. Nana C, Moschetta JM, Bénard E, et al. Experimental and numerical analysis of quiet MAV rotors. In: *The 50th 3AF international conference on applied aerodynamics*.
25. Sinibaldi G and Marino L. Experimental analysis on the noise of propellers for small UAV. *Appl Acoust* 2013; 74: 79–88.
26. Rozenberg Y, Roger M and Moreau S. Rotating blade trailing-edge noise: experimental validation of analytical model. *AIAA J* 2010; 48: 951–962.
27. Kim YN and George AR. Trailing-edge noise from hovering rotors. *AIAA J* 1982; 20: 1167–1174.
28. Blandeau V. *Aerodynamic broadband noise from contra-rotating open rotors*. PhD Thesis, University of Southampton, UK, 2011.
29. Alhérière PA, Olivanti R, Lustosa L, et al. Nonlinear control of a particular tilt-body MAV: the Roll & Fly. In: *The 24th Mediterranean conference on control and automation*.
30. Leishman JG. *Principles of helicopter aerodynamics*. Cambridge: Cambridge University Press, 2002.
31. Amiet RK. Acoustic radiation from an airfoil in a turbulent stream. *J Sound Vib* 1975; 41: 407–420.
32. Marié S and Sagaut P. Comparison between lattice Boltzmann method and Navier–Stokes high order schemes for computational aeroacoustics. *J Comput Phys* 2009; 228: 1056–1070.
33. Gourdain N, Jardin T, Serré R, et al. Application of a lattice Boltzmann method to some challenges related to micro-air vehicles. *Int J Micro Air Veh* 2018; 10: 285–299.
34. Robinson SK. Coherent motions in the turbulent boundary layer. *Annu Rev Fluid Mech* 1991; 23: 601–639.
35. Head MR and Bandyopadhyay P. New aspects of turbulent boundary-layer structure. *J Fluid Mech* 1981; 107: 297–338.
36. Gourdain N, Serré R, Jardin T, et al. Analysis of the flow produced by a low-Reynolds rotor optimized for low noise applications. Part I: aerodynamics. In: *The 43rd European Rotorcraft Forum*.
37. George WK. *Lectures in turbulence for the 21st century*. Göteborg: Chalmers University of Technology, 2013.
38. Fukano T, Kodama Y and Senoo Y. Noise generated by low pressure axial flow fans, I: modeling of the turbulent noise. *J Sound Vib* 1977; 50: 63–74.
39. Soderman PT. Leading-edge serrations which reduce the noise of low-speed rotors. NASA Technical Note No. D-7371, 1973.
40. Favier J, Pinelli A and Piomelli U. Control of the separated flow around an airfoil using a wavy leading edge inspired by humpback whale flippers. *C R Mecanique* 2012; 340: 107–114.
41. Clair V, Polacsek C, Le Garrec T, et al. Experimental and numerical investigation of turbulence-airfoil noise reduction using wavy edges. *AIAA J* 2013; 51: 2695–2713.
42. Lyu B, Azarpeyvand M and Sinayoko S. Noise prediction for serrated leading-edges. In: *The 22nd AIAA/CEAS aeroacoustics conference*, paper no. AIAA-2016-2740.
43. Chaitanya P, Joseph P, Narayanan S, et al. Performance and mechanism of sinusoidal leading edge serrations for the reduction of turbulence–aerofoil interaction noise. *J Fluid Mech* 2017; 818: 435–464.
44. Serré R, Gourdain N, Jardin T, et al. Analysis of the flow produced by a low-Reynolds rotor optimized for low noise applications. Part II: acoustics. In: *The 43rd European Rotorcraft Forum*.
45. Wang J, Zhang C, Wu Z, et al. Numerical study on reduction of aerodynamic noise around an airfoil with biomimetic structures. *J Sound Vib* 2017; 394: 46–58.